International Journal of
MATERIALS RESEARCH

Zeitschrift für METALLKUNDE

Original Contributions

D. Tolnai[a], T. Sosro[a,b], S. Gavras[a], R. H. Buzolin[c], N. Hort[a]
[a] Magnesium Innovation Centre, Helmholtz Zentrum Geesthacht, Geesthacht, Germany
[b] Brunel Centre for Advanced Solidification Technology, Brunel University London, United Kingdom
[c] Institute of Materials Science, Joining and Forming, Graz University of Technology, Graz, Austria

# In-situ synchrotron investigation of the phases- and their morphology-development in Mg–Nd–Zn alloys

*Paper presented at the Symposium "Tomographic and Radiographic Imaging with Synchrotron X-rays and Neutrons" of the MSE 2018, 26 – 28 September 2018, Darmstadt, Germany*

The addition of Zn to the Mg–Nd system improves the yield strength and creep resistance, however its influence on the intermetallic phases in the ternary system is not yet fully understood. Understanding the sequence of phase-formation and phase-evolution during solidification and processing is essential to microstructure design. The solidification was investigated with in-situ synchrotron radiation-diffraction and tomography during cooling from the molten state to 200 °C to investigate the phase-formation and transformation characteristics. The solidification starts with α-Mg followed by two distinct intermetallic phases T2 and T3. The results suggest that Zn stabilizes the $Mg_3Nd$ phase and accelerates precipitate formation. The dendritic morphology changes during solidification towards coarser shapes, thus impedes feeding and promotes hot tearing.

**Keywords:** MgNdZn alloys; In situ; Solidification; Synchrotron diffraction; Synchrotron tomography

## 1. Introduction

The growing application of light weight solutions in the transportation industries requires low density materials with high specific mechanical properties. Furthermore, the absolute properties in the material's property profile should be sufficient to meet the demands of the application at hand. Mg, owing to its low density, fulfils the first requirement [1] and also the latter in most cases as a result of large-scale alloy development efforts [2]. This enables the substitution of heavier counterparts with Mg products. The degradation of Mg alloys under physiological conditions allows applying specific alloys as implant materials without the need of subsequent removal surgery [3].

Alloys of the Mg–Zn system possess enhanced strength and ductility [4] which made ZK60 (Mg-6.0Zn-0.6Zr (wt.%)) one of the most widely used commercial wrought Mg alloys. Owing to this enhancement, this system has been the basis for *RE* (rare earth) additions aiming to further improve the mechanical property profile through the formation of grain boundary particles [5]. Due to their price, low solid solubility *RE* elements have gained attention because relatively low concentrations are sufficient to introduce secondary phase particles. Neodymium with a maximum solid solubility of 3.6 wt.% at 549 °C [6] became the focus of numerous pieces of research because it is an ideal element to further improve strength at elevated temperatures [7, 8]. In order to characterize the phases in the Mg–Zn–

Nd system Calphad [9] and first principle studies [10] have been performed. The microstructure property relationship has been investigated for different processing routes e. g. high cycle fatigue [11], hot compression [12] and equal channel angular pressing [12]. Furthermore, due to the low cytotoxicity of Nd the Mg–Nd–Zn system is also considered as a prospective alloy for bio-absorbable implants [14].

Phase formations and transformations in materials are revealed in in-situ diffraction experiments during solidification as a function of temperature and time [15]. The validation of existing phase diagrams and the development of more precise thermodynamic databases is achieved by the identification of secondary phases and the determination of their solidification sequences [16]. The use of neutron sources provides better statistics, due to the relatively large sample size in comparison to synchrotron sources [17]. However, it should be noted that synchrotron sources yield superior time–temperature resolution [18], which allows for the modelling of more realistic casting conditions with the experiments.

The continuous development of image acquisition by synchrotron X-ray imaging [19] allows following the solidification process in situ. For instance, a thin plate-like sample is used as a specimen and radiographs can be taken with short acquisition times during solidification providing excellent time resolution [20]. To melt the sample, a Bridgman furnace is commonly used, which provides a well-defined solidification front and solidification rate. The disadvantage of this method is that it only delivers two-dimensional information. By rotating the sample during solidification, tomography can be performed [21]. In order to perform in-situ tomographic investigations, the scan must be done faster than the evolution of the microstructure. By cooling down the sample to the solid state the whole solidification sequence can be acquired in 3 dimensions [22, 23].

The aim of this research is to investigate the phase formation during solidification in Mg–Nd–Zn alloys with synchrotron radiation diffraction to characterize the phases as a function of temperature and with synchrotron radiation tomography to follow the evolution of the internal phase morphologies.

## 2. Experimental procedure

The alloys investigated were cast by permanent mold indirect chill casting [24]. Pure Mg was melted in an electric resistance furnace under a protective atmosphere with a mixture of Ar and 2 vol.% $SF_6$. The Nd and Zn were added in pure form, while the melt was continuously stirred. The melt was held at 750 °C for 10 min, then poured into a preheated steel mold (660 °C). The crucible with the molten alloy was held at this temperature for 15 min and subsequently immersed into a room temperature water bath at a rate of $10\ \mathrm{mm} \cdot \mathrm{s}^{-1}$.

Three alloy compositions were investigated in this work; Mg5Nd3Zn, Mg5Nd5Zn and Mg5Nd7Zn. All alloy compositions described in this work are stated in wt.%, unless it is stated otherwise. The actual compositions of the alloys were measured with a Spectrolab spark analyzer. The Nd content was also measured using a Brucker S5 X-ray fluorescence (XRF) to determine the exact amounts of Nd in the investigated alloys.

Specimens for scanning electron microscopy (SEM) analysis were prepared by grinding and polishing using SiC paper and OPS solution respectively. A TESCAN Vega SB-U III SEM with an accelerating voltage of 15 kV and working distance of 15 mm were used for microstructural characterization.

The in-situ synchrotron radiation diffraction experiments were performed at the P07 (HEMS) beamline of Petra III. DESY (Deutsches Elektronen-Synchrotron) A monochromatic beam was used with the energy of 100 keV ($\lambda = 0.0124$ nm) and a cross-section of $(1.1\ \mathrm{mm})^2$. The acquisition time of each diffraction pattern was set to 0.5 s. The samples were enclosed in Mettler Toledo stainless steel crucibles (ME 29990) under Ar atmosphere. The experiments were performed in the chamber of a modified DIL 805 A/D (Bähr-Thermoanalyse GmbH, Hüllhorst, Germany) dilatometer; the sides of the chamber were covered with Kapton windows and the coil was modified so the beam passed through the sample only. The diffraction patterns (Debye–Scherrer rings) were recorded by a Perkin Elmer 1622 Flatpanel detector with an effective pixel size of $(200\ \mu\mathrm{m})^2$ placed 1 603 mm behind the sample, calibrated by an $LaB_6$ standard powder sample. The samples were heated at a constant rate of 50 and $100\ \mathrm{K\ min}^{-1}$ up to 800 °C then held for 5 min to ensure temperature homogeneity and subsequently cooled with the same rate to 200 °C. The diffraction patterns were integrated azimuthally and analyzed with the software Fit2D. Line profiles were obtained by integrating the diffraction patterns in the azimuthal direction.

The in-situ synchrotron tomography experiment was carried out at Swiss Light Source (Paul Scherrer Institute, Villigen, Switzerland) using the TOMCAT beamline. The radiographies were acquired with a rate of 2.5 ms with a PCO-DIMAX CMOS camera. The data were reconstructed to images with dimensions of $1\,008 \times 1\,008 \times 808$ pixels with a voxel size of $(3\ \mu\mathrm{m})^3$. The quantitative analysis was performed on cropped volumes of $400 \times 400 \times 300$ pixels. More details of the experimental setup, data acquisition settings and image processing steps have been provided in previous work [25]. The mean and product of the principal curves, mean (K) and Gauss curvatures (H), were determined using α-Mg dendrites during solidification with Avizo® software. A triangular approximation prior to calculation was used to produce a surface of the voxel-based volume of the segmented phase. For each triangle of the

Table 1. Chemical composition of the investigated samples.

| Nominal composition | Nd wt.% (spark) | Nd wt.% (XRF) | Zn wt.% (spark) |
|---|---|---|---|
| Mg5Nd3Zn | >4.20 | 4.35 | 3.20 |
| Mg5Nd5Zn | >4.20 | 4.20 | 5.20 |
| Mg5Nd7Zn | >4.20 | 4.34 | 8.00 |

rendered surface, the osculant curves were determined taking into consideration the neighbouring triangles up to the fifth order. The local radii of these curves were averaged five times with the radii of direct neighbour triangles before the reciprocal of the local radius was calculated. In order to prevent phases cut by the boundaries of the region of interest, surfaces that simultaneously exhibited zero values for mean and Gauss curvatures were excluded from further evaluation.

## 3. Results and discussion

The actual chemical compositions of the alloys measured by XRF and spark analysis are listed in Table 1.

The chemical compositions of the alloys are close to the intended compositions, however, in the case of Mg5Nd7Zn, the Zn content is 1 wt.% higher. In the case of small alloy batches this is within the tolerance of the composition. The backscattered electron (BSE) micrographs of the alloys are shown in Fig. 1.

In all the alloys two distinct intermetallic morphologies can be distinguished. One of them is a continuous intermetallic phase, the other one is more lamella-like. The increase in Zn content besides increasing the overall volume fraction of the intermetallics also increases the proportion of the lamella like intermetallic phase. The Debye–Scherrer patterns acquired during the in-situ solidification test of Mg5Nd5Zn are shown in Fig. 2.

At 700 °C the alloy is completely molten. The crystalline peaks originate from the stainless steel crucible, while the diffuse background ring is from the melt. At 639 °C besides the crucible some diffraction peaks from the α-Mg can be

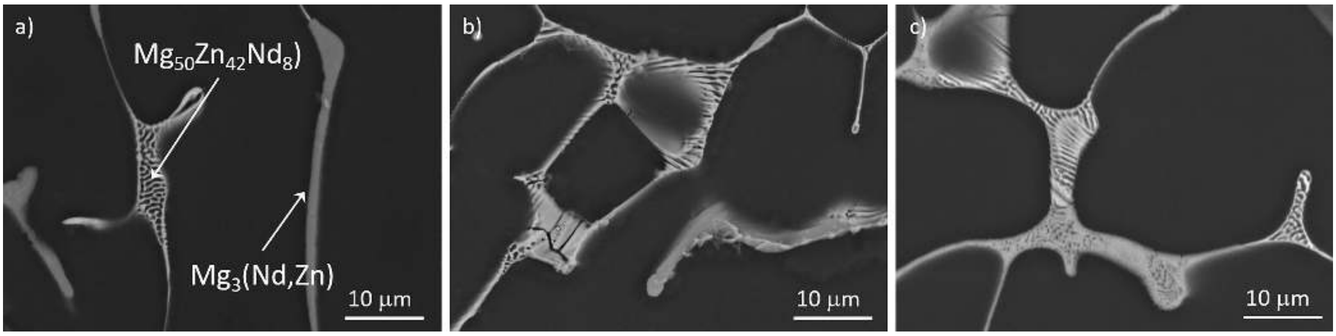

Fig. 1. BSE micrographs of the investigated alloys: (a) Mg5Nd3Zn, (b) Mg5Nd5Zn, and (c) Mg5Nd7Zn.

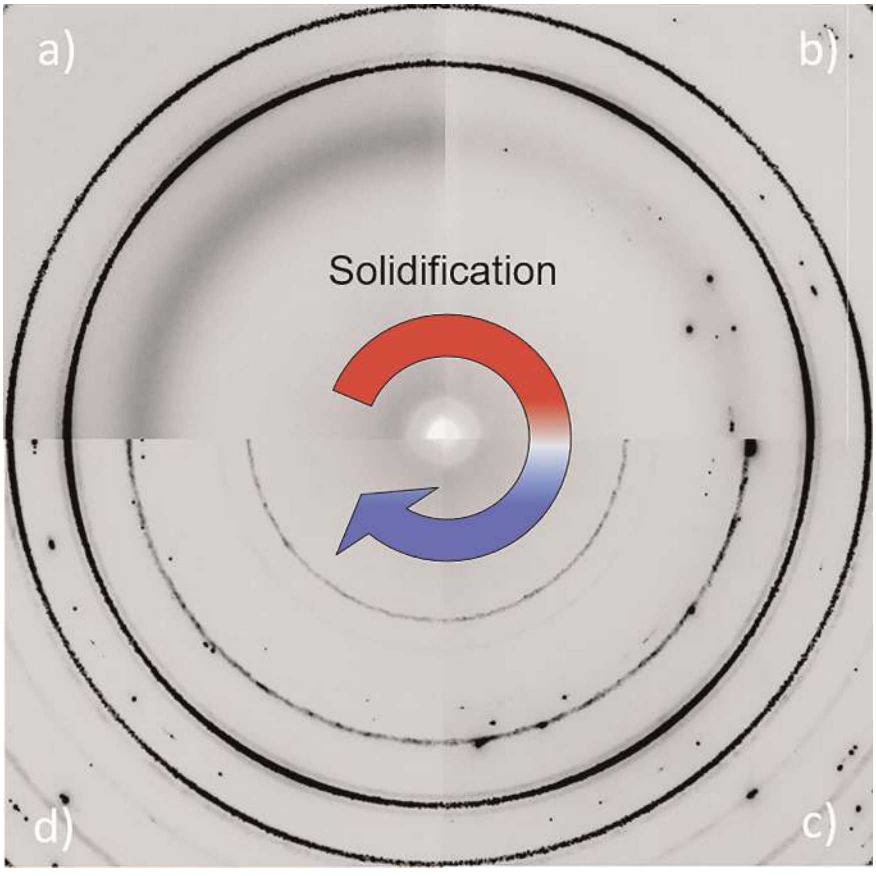

Fig. 2. Debye–Scherrer patterns acquired during the in situ solidification test of Mg5Nd5Zn at: (a) 700 °C, (b) 639 °C, (c) 510 °C, and (d) 470 °C.

observed, while the diffuse background loses its intensity as the amount of the melt decreases. The α-Mg peaks appear and disappear as the crystallines fulfil the Bragg equation while floating in the melt. At 510 °C the solidification of Mg proceeds, while the signal of the melt disappears, indicating that its volume fraction becomes close to the detection limit. A peak from the intermetallics can be seen. At 470 °C the solidification is complete. The comparison of the integrated line profiles at RT along with the line profiles acquired by integration of the Debye–Scherrer patterns from the investigated alloys are shown in Fig. 3. The accuracy of the temperature measurement of the experimental setup is 1 K. However, as the phase begins to form, their observation is dependent on the detection limit of the diffraction. Therefore, it is most likely that at the very beginning when the phase has a low volume fraction and the crystallites only occasionally fulfil the Bragg equation the detection is limited.

The comparison of the alloys at RT in the as-cast state shows that the Mg5Nd3Zn consists of the $Mg_3(Nd,Zn)$ (T3 phase, fcc) besides the α-Mg, while the higher Zn containing alloys consist of $Mg_{50}Zn_{42}Nd_8$ (tetragonal crystal structure) as well which is known as the T2 phase in the literature. However, from the BSE micrograph of Mg5Nd3Zn in Fig. 1a two intermetallic morphologies can be clearly distinguished. The volume fraction of the $Mg_{50}Zn_{42}Nd_8$ intermetallic with the lamella-like structure must be low, close to the detection limit, therefore it might be difficult to observe it with synchrotron radiation diffraction in a measurement setup, where the sample is stationary. The integrated line profiles show similar solidification behavior for all the alloys. The red profiles represent the liquid state. The hump originates from the amorphous background signal, while the crystalline peaks originate from the steel crucibles. On the second profiles (green) besides the crucibles, peaks can be observed from the primary Mg dendrites. On the third profiles (blue) these are complemented by the peaks of the intermetallic phases. The last profiles are integrated from the Debye–Scherrer patterns acquired at the end of the experiment at 200 °C. The peaks move towards higher *q* val-

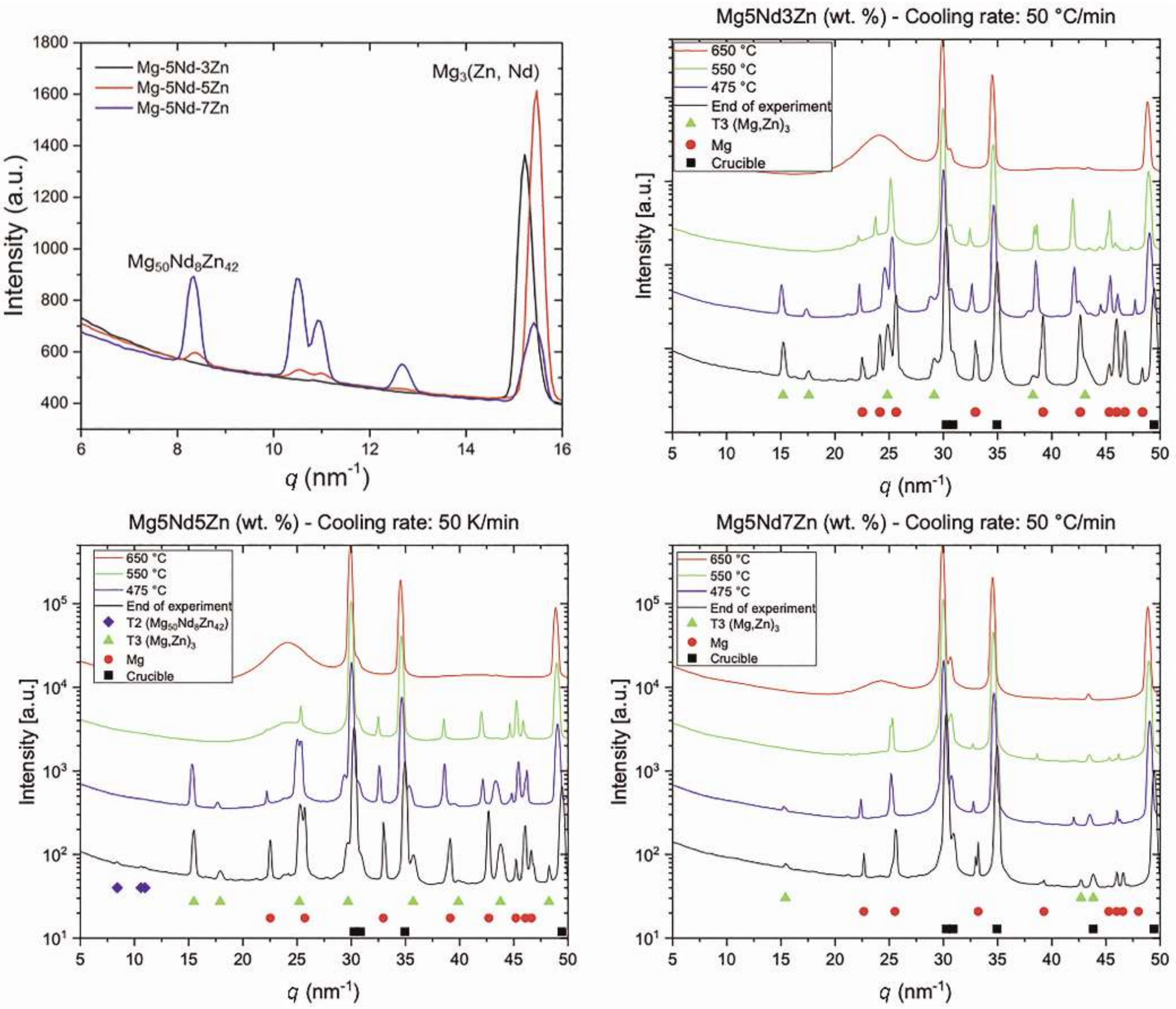

Fig. 3. Comparison of the alloys at RT in as-cast condition and line profiles of the investigated alloys acquired during cooling.

ues because of the decrease in lattice parameter while cooling down. The summary of the formation temperatures of the different phases obtained by synchrotron radiation diffraction are listed in Table 2.

Tomographic slices of the microstructure of Mg5Nd5Zn at different temperatures and the reconstructed 3D image of the different phases are shown in Fig. 4.

The in-situ tomographic experiment provides information regarding the evolution of the internal architecture during solidification. In these images the green colour represents the dendritic structure, and blue the interdendritic space, which is liquid during cooling, until the structure becomes completely solid at 500 °C. Since there is a necessity of continuous rotation during the scan, a thermocouple cannot be fixed on the sample. The temperature is measured with a pyrometer, which has a high inaccuracy at this relatively low temperature. Therefore, the temperature has been scaled with ex-situ DTA measurements. The quantitative analysis of the structure could only be performed after the dendritic coherency point, the temperature where an internal skeleton of α-Mg dendrites has built up. This hinders the movement of the solidified particles, thus enables the proper reconstruction of the volume. Pores were only observed at the end of solidification, which is expected as the network of solidified phase forms a complex feeding path. This obstructs the healing by the remaining liquid phase and pores form. The results of the quantitative analyses are shown in Fig. 5.

The volume fraction of Mg naturally increases during cooling, while the amount of intermetallics (including melt in the liquid phase) decreases as the solidification proceeds. As the structure becomes solid to a point where sufficient feeding is not possible anymore, pores appear. The dendrites were characterized with the mean and Gauss curvatures, the mean and the product of the principal curvatures (largest and smallest curvature at any given surface point). The values are representative of a given surface form allowing characterization of the morphology of the dendrites statistically. At 537 °C the distribution has three maxima in the positive–positive quadrant and close to the origin. This represents mostly spheroid-like shapes and flatter surfaces describing the shape of the dendrites shortly after their coherency point. As the cooling proceeds, one maximum disappears and the distribution shifts towards concave shapes. At 509 °C only one peak in the distribution is left which means that the structure

Table 2. Formation temperatures of the phases.

| | Mg5Nd3Zn | Mg5Nd5Zn | Mg5Nd7Zn |
|---|---|---|---|
| α-Mg | 631 ± 2 °C | 619 ± 2 °C | 617 ± 2 °C |
| $Mg_3(Nd,Zn)$ | 507 ± 2 °C | 485 ± 2 °C | 483 ± 2 °C |
| $Mg_{50}Zn_{42}Nd_8$ | N/A | 467 ± 2 °C | N/A |

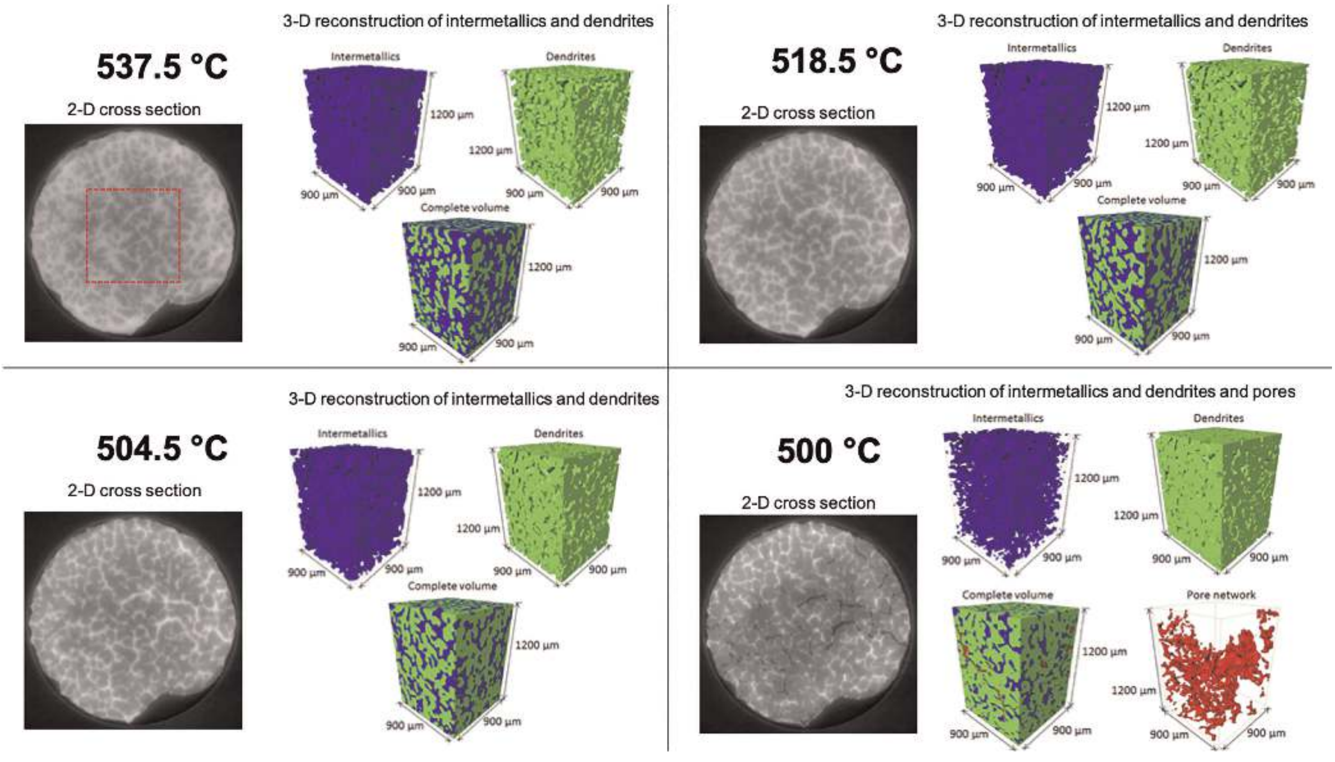

Fig. 4. Tomographic slices of the microstructure of Mg5Nd5Zn at different temperatures and the reconstructed 3D image with the phases segmented.

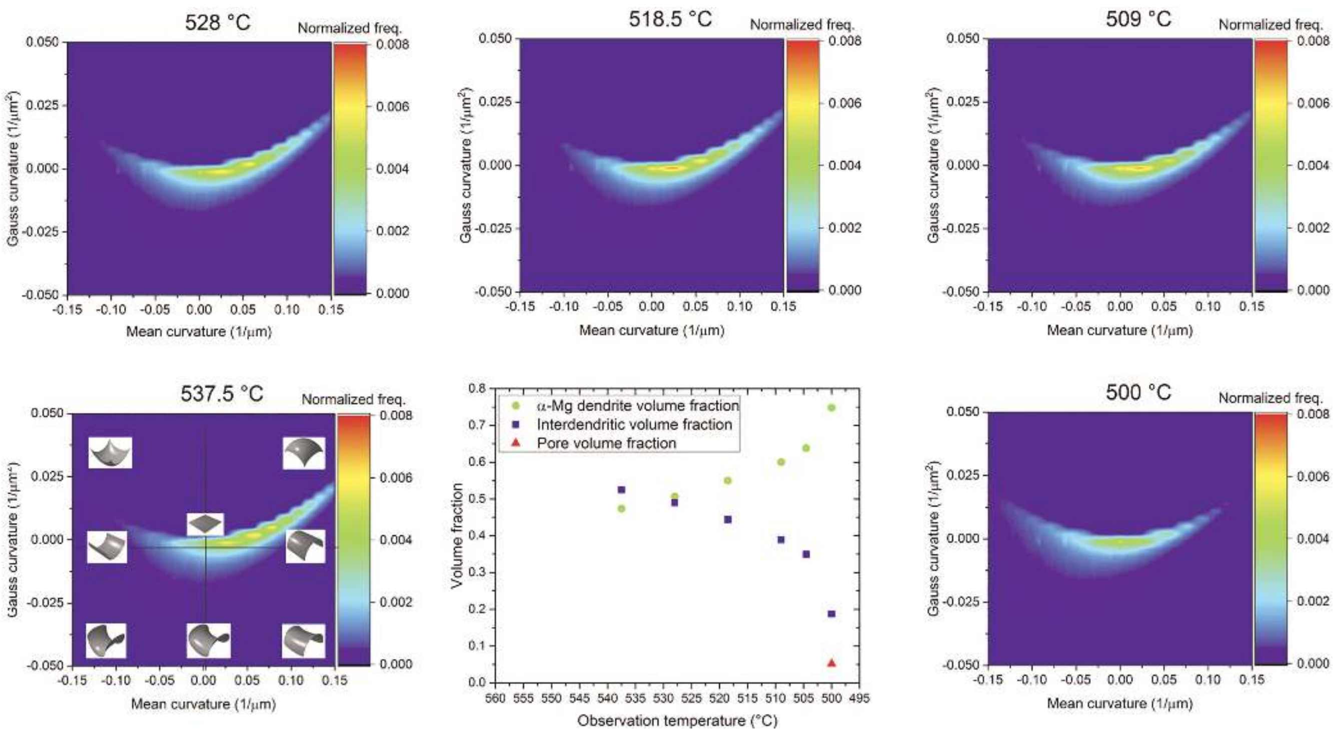

Fig. 5. Volume fraction of the segmented phases, changes of dendrite morphologies at different temperatures during cooling.

coarsens further. As the solidification finishes the morphology can be described mostly with convex and concave spheroid-like shapes indicating a coarse dendritic structure with relatively short dendrite arms compared to their thickness.

## 4. Conclusions

The solidification properties of Mg-5Nd-*x*Zn alloys were investigated with in-situ synchrotron radiation diffraction and tomography. From the findings the following main conclusions can be drawn.

- The solidification sequence of the alloys starts with the formation of the α-Mg dendrites followed by solidification of intermetallics.
- The dendritic structure coarsens during cooling, and in the final stage pores appear, most likely due to poor feeding.
- The presence of Zn stabilizes the $Mg_3(Nd, Zn)$ phase, which is meta-stable in the binary Mg–Nd alloys. Furthermore, it promotes the formation of the $Mg_{50}Zn_{42}Nd_8$ phase.

This research was funded by Deutsche Forschungsgemeinschaft under the grants TO817/4-1 and ME4487/1-1 The authors acknowledge the Deutsches Elektronen-Synchrotron and the Paul Scherrer Institut for the provision of facilities of the TOMCAT beamline at SLS within the framework of the proposals I-20150471 and 20150382.

### References

[1] M. Pekguleryuz, K.U. Kainer, A. Kaya: Fundamentals of magnesium alloy metallurgy, Woodhead: Philadelphia (2013). DOI:10.1533/9780857097293

[2] M.M. Avedesian, H. Baker: Magnesium and magnesium alloys, ASM Specialty Handbook, ASM International: USA (1999).

[3] F. Feyerabend, J. Fischer, J. Holtz, F. Witte, R. Willumeit, H. Drücker, C. Vogt, N. Hort: Acta Biomater. 6 (2010) 1834. DOI. 10.1016/j.actbio.2009.09.024. PMid:19800429

[4] S.M. He, L.M. Peng, X.Q. Zeng, W.J. Ding, Y.P. Zhu: Mater. Sci. Eng. A 433 (2006) 175. DOI:10.1016/j.msea.2006.06.063

[5] Q. Li, Q. Wang, Y. Wang, X. Zeng, W. Ding: J. Alloys Compd. 427 (2007) 115. DOI:10.1016/j.jallcom.2006.02.054

[6] L.L. Rokhlin: Magnesium Alloys Containing Rare Earth Metals Taylor&Francis: London, UK (2003) ISBN 0-415-28414-7.

[7] P.H. Fu, L.M. Peng, H.Y. Jiang, J.W. Chang, C.Q. Zhai: Mat. Sci. Eng. A 486 (2008) 183. DOI:10.1016/j.msea.2007.08.064

[8] D. Wu, R.S. Chen, W. Ke: Mater. Des. 58 (2014) 324. DOI:10.1016/j.matdes.2014.01.061

[9] H.Y. Qi, G.X. Huang, H. Bo, G.L. Xu, L.B.Liu, Z.P. Jin: J. Alloys Compd 509, (2011) 3274. DOI:10.1016/j.jallcom.2010.07.056

[10] D. Wang, M. Amsler, V.I. Hegde, J.E. Saal, A. Issa, B. Zhou, X. Zeng, C. Woverton: Acta Mater. 158 (2018) 65. DOI:10.1016/j.actamat.2018.07.041

[11] Z.M. Li, P.H. Fu, L.M. Peng, Y.X. Wang, H.Y. Jiang, G.H. Wu: Mat. Sci. Eng. A 579 (2013) 170. DOI:10.1016/j.msea.2013.05.040.

[12] W. Wu, L. Jin, J. Dong, W. Ding: Trans. Nonferoous Met. Soc. China 22 (2012) 1169. DOI:10.1016/S1003-6326(11)61301-0

[13] S. Zhao, E. Guo, G. Cao, L. Wang, Y. Lun, Y. Feng: J. Alloys Compd. 705 (2017) 118. DOI:10.1016/j.jallcom.2017.02.122

[14] J. Zhang, H. Li, W. Wang, H. Huang, J. Pei, H. Qu, G. Yuan, Y. Li: Acta Biomater. 69 (2018) 372. DOI:10.1016/j.actbio.2018.01.018

[15] D. Tolnai, C.L. Mendis, A. Stark, G. Szakács, B. Wiese, K.U. Kainer, N. Hort: Mat. Lett. 102–103 (2013) 62. DOI:10.1016/j.matlet.2013.03.110

[16] B. Wiese, C.L. Mendis, D. Tolnai, A. Stark, N. Schell, H-P. Reichel, R. Brückner, K.U. Kainer, N. Hort: J. Alloys Compd. 618 (2015) 64. DOI:10.1016/j.jallcom.2014.08.151

[17] E. Vandersluis, D. Sediako, C. Ravindran, A. Elsayed, G. Byczynski: J. Alloys Compd. 736 (2018) 172. DOI:10.1016/j.jallcom.2017.11.118

[18] G. Garces, D.G. Morris, M.A. Muñoz-Morris, P. Perez, D. Tolnai, C.L. Mendis, A. Stark, H.K. Lim, S. Kim, N. Schell: Acta Mater. 94 (2015) 78. DOI:10.1016/j.actamat.2015.04.048

[19] J.C. Labiche, O. Mathon, S. Pascarelli, M.A. Newton, G.G. Ferre, C. Curfs, G. Vaughan, A. Homs, D.F. Carreiras: Rev. Sci. Instrum. 78 (2007). 091301. DOI:10.1063/1.2783112

[20] R.H. Mathiesen, L. Arnberg, F. Mo, T. Weitkamp, A. Snigirev: Phys. Rev. Lett. 83 (1999) 5062. DOI:10.1103/PhysRevLett.83.5062
[21] O. Ludwig, M. Di Michiel, L. Salvo, M. Suéry, P. Falus: Mat. Trans. A 36 (2005) 1515. DOI:10.1007/s11661-005-0243-8
[22] N. Limodin, L. Salvo, E. Boller, M. Suéry, M. Felberbaum, S. Gailliègue, K. Madie: Acta Mater. 57 (2009) 2300. DOI:10.1016/j.actamat.2009.01.035
[23] S. Terzi, J.A. Taylor, Y.H. Cho, L.Salvo, M.Suéry, E.Boller, A.K. Dahle: Acta Mater. 58. (2010) 5370. DOI:10.1016/j.actamat.2010.06.012
[24] F.R. Elsayed, N. Hort, M.A. Salgado Ordorica, K.U. Kainer: Mater. Sci. Forum. 690, 65. (2011) DOI:10.4028/www.scientific.net/MSF.690.65
[25] T. Subroto, C.L. Mendis, F. D'Elia, G. Szakács, J.L. Fife, N. Hort, K.U. Kainer, D. Tolnai: Magnesium Technology 2017, (2017) 605. DOI:10.1007/978-3-319-52392-7_83

(Received October 30, 2018; accepted February 11, 2019; online since June 5, 2019)

**Correspondence address**

Dr. Domonkos Tolnai
Helmholtz Zentrum Geesthacht
Max-Planck-Straße 1
21502 Geesthacht
Germany
E-mail: domonkos.tolnai@hzg.de
Tel.: +49 4152 87-1974

**Bibliography**

DOI 10.3139/146.111786
Int. J. Mater. Res. (formerly Z. Metallkd.)
111 (2020) 1; page 4 – 10

ISSN 1862-5282